

Study on the Photoelectric Hot Electrons Generation and Transport
with Metallic-Semiconductor Photonic Crystals

by

Yu Wang

B.S., Physics, National Taiwan University, Taiwan (2010)

M.S., Materials Science and Engineering, National Taiwan University, Taiwan (2012)

Submitted to the Department of Materials Science and Engineering
in Partial Fulfillment of the Requirements for the Degree of

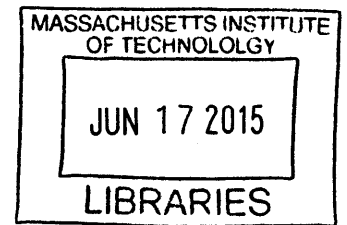
Master of Science

at the

Massachusetts Institute of Technology

June 2015

ARCHIVES



© 2015 Massachusetts Institute of Technology. All rights reserved

Signature redacted

Signature of Author

Department of Materials Science and Engineering
May 21, 2015

Signature redacted

Certified by

Sang Gook Kim
Professor of Mechanical Engineering
Thesis Supervisor

Signature redacted

Certified by

Harry Tuller
Professor of Materials Science and Engineering
Thesis Reader

Signature redacted

Accepted by.....

Donald R. Sadoway
Chair, Departmental Committee on Graduate Students

Study on the Photoelectric Hot Electrons Generation and Transport with Metallic-Semiconductor Photonic Crystals

by

Yu Wang

Submitted to the Department of Materials Science and Engineering
on May, 22 in Partial Fulfillment of the Requirements for the Degree of
Master of Science in Materials Science and Engineering

Abstract

Photoelectric hot carrier generation in metal-semiconductor junctions allows for optical-to-electrical energy conversion at photon energies below the bandgap of the semiconductor. Which opens new opportunities in optical sensors and energy conversion devices. In this thesis research, the wafer-scale metallic-semiconductor photonic crystal (MSPhC) has been designed for photoelectric hot electrons collection. The periodic nanocavities structure of MSPhC supports various optical modes that can resonate with light in broad wavelength region.

Optical simulation and experimental results of MSPhC have been demonstrated. The simulation results shows MSPhC can achieve up to 70% absorption in the solar radiation range, with ultra-thin metal film. Experimentally, MSPhC has fabricated via 6" Si wafer scalable microfabrication techniques. A broadband sub-bandgap hot electron response with a full width at half maximum (FWHM) of 235 nm centered at 590 nm is observed. Photoresponse enhancement factor of 12.28 at 639 nm compared to a flat chip is also measured. Applications of these results could lead to low-cost and robust photo-electrochemical device such as full-spectrum solar water splitting.

Thesis Supervisor: Sang Gook Kim

Title: Professor of Mechanical Engineering

Table of Contents

Abstract	3
Table of Contents	5
List of Figures	7
Chapter 1 Introduction	11
1.1 Photoelectric Hot Electrons for Sub-bandgap Absorption	11
1.2 Metallic-Semiconductor Photonic Crystals.....	11
Chapter 2 Theoretical Background	14
2.1 Photonic Crystals.....	14
2.2 Hot Electrons.....	15
Chapter 3 Device Design	17
3.1 Structure Design	17
3.2 Factors Affecting Hot Electrons Injection Efficiency	18
3.2.1 Generation: Band Structure and Density of States	18
3.2.2 Transport: Mean free path	20
3.2.3 Injection: Electron Momentum.....	20
Chapter 4 Optical Simulation	22
4.1 Finite-difference Time-domain (FDTD) Simulation	22
4.1.1 FDTD Models and Methods.....	22
4.1.2 Strength of FDTD.....	23

4.2	FDTD Simulation of MSPhC	24
4.3	Structural Parameters Dependence.....	25
4.4	Absorption Contribution Analysis.....	29
4.5	Modes Analysis	31
Chapter 5 Preliminary Experimental Results.....		36
5.1	Fabrication Process.....	36
5.1.1	Nanocavity Array.....	36
5.1.2	Metal and Semiconductor Layers.....	37
5.2	Device Characterization Methods	38
5.2.1	Imaging.....	38
5.2.2	I-V curve and Photoresponse.....	39
5.3	Images of Fabricated Device	39
5.4	Reflection Spectrum	40
5.5	Diode Characteristics.....	41
5.6	Wavelength Dependent Photoresponse	42
Chapter 6 Summary and Future Works.....		45
Reference		47

List of Figures

Fig. 1.1	(a) and (b) Schematic diagram of the Metal-Dielectric Photonic Crystals (MDPhC) structure. (c) The total measured and simulated absorption spectrum for MDPhC. (d) Contour plot of the RCWA simulated absorption spectrum as a function of incident angle θ . [6]..... 12
Fig. 2.1	Schematic diagram of simple examples for 1D, 2D, 3D photonic crystals. Different colors represent materials with different dielectric constants. [7] 14
Fig. 2.2	Hot electrons can be injected into a semiconductor by forming a Schottky barrier with the plasmonic nanostructure. Hot electrons with energies high enough to overcome the Schottky barrier $\phi_{SB} = \phi_M - \chi_S$ are injected into the conduction band E_c of the neighboring semiconductor, where ϕ_M and χ_S are the metal work function and the semiconductor electron affinity. [11].....16
Fig. 3.1	Schematic diagram of (a) cross section of designed MSPhC, and (b) the process of subsequent light absorption, hot electron generation and collection.18
Fig. 3.2	Density of state for free electron model. Hot electron excited from $EF - \hbar\omega$ to EF can have energy distributed from EF to $EF + \hbar\omega$. Within it, hot electron in blue line shaded area (excited from orange line shaded area) have sufficient energy to across schottky barrier.19
Fig. 3.3	Schematic diagram of the effective cone for hot electron injection in k space.21
Fig. 4.1	Reflection, transmission, and absorption (RTA) spectrum of MSPhC (Structure parameters are chose base on experimental values: cavity radius:

	320nm, periodicity: 840nm, depth: 1 μ m, Au layer: 13nm, TiO ₂ : 75nm, Al ₂ O ₃ : 50nm).....	25
Fig. 4.2	Simulated (a) Cavity radius r , (b) Cavity depth d , and (c) Cavity periodicity a dependent total absorption. Where r is varied from 167 to 1000nm, d is varied from 250 to 1500 nm, and a is varied from $2r$ to $4r$	27
Fig. 4.3	Simulated (a) Al ₂ O ₃ , (b) TiO ₂ , and (c) Au thickness dependent total absorption.	28
Fig. 4.4	Simulated images of (a) electric field intensity and (b) special power absorption, at incident wavelength of 752 nm.....	30
Fig. 4.5	Simulated spectra of (a) ratio of absorption contribution, and (b) total absorption of each materials in MSPhC	30
Fig. 4.6	FDTD simulated absorption in both Au and TiO ₂ as a function of Au thickness.	31
Fig. 4.7	Optical modes that MSPhC can possibly support: (a) cavity mode, (b) gap mode, (c) waveguide mode, (d) surface plasmon mode. Red figures represent electric field intensity of coupled light.	32
Fig. 4.8	(a) Cross sectional diagram and (b) top view of simulation unit with 10 randomly positioned broad band dipole sources with polarization out of plane (blue dots and arrows), and 8 1D time monitors (yellow lines).	33
Fig. 4.9	Amplitude to wavelength figure by summing up all 8 time monitors with varying Au film thickness of 13, 26, 52nm.	34
Fig. 4.10	Simulated E-field intensity image at (a) 500nm, (b) 600nm, and (c) 700nm. Which corresponds to waveguide mode, surface plasmon mode, and cavity mode.	35
Fig. 5.1	Schematic diagram of wafer-scale MSPhC fabrication process.....	38

Fig. 5.2	(a) SEM image of Al ₂ O ₃ shells. (b) Top view and (c) cross section view at 30° angle of fully fabricated device with TiO ₂ and Au layers deposited. (d) Photo image of 1cm by 1cm device.	40
Fig. 5.3	UV-Vis reflection measurements at the 10 nm Au and TiO ₂ surfaces on the MSpHC.....	41
Fig. 5.4	Measured I-V curves of MSpHC (a) with and (b) without Al ₂ O ₃ passivation layer at Au/TiO ₂ interface.....	42
Fig. 5.5	(a) Measured high-resolution photoresponse of MSpHC. (b) Laser diode short-circuit photoresponse measurements at various Au thicknesses of 10 nm, 20 nm, and 30 nm. The black curve is our best reported device with no ITO layer. The green curve is a flat chip with identical films for comparison.	44

Chapter 1 Introduction

1.1 Photoelectric Hot Electrons for Sub-bandgap Absorption

Many semiconductor devices that convert solar energy to electrical energy have been developed, but there is fundamental limitation on the spectral range and efficiency due to the threshold of light absorption at the bandgap energy. Adding a second material interfaced with the semiconductor opens up the possibility to take advantage of sub-bandgap photons. In this case, the sub-bandgap photon can be absorbed in the second material. An excited “hot” electron or hole then injects into the semiconductor and be collected. The term hot electron refers to an electron that is not in thermal equilibrium with the electron gas but has energy higher than expected from thermal distribution. It has recently been demonstrated that nanometer-scale metallic particles or antennas with a surface plasmon resonance can enhance this sub-bandgap absorption which leads to increased efficiencies and spectral selectivity [1]-[4]. The possibility to capture the energy normally lost to heat would open new opportunities in optical sensors and energy conversion devices. Especially in the field of photo electrochemistry, direct utilization of the hot carrier energy would be very useful, since the stable semiconductor materials are typically oxides with wide bandgaps which absorb little of the solar spectrum [5].

1.2 Metallic-Semiconductor Photonic Crystals

Previous study in our group showed that the designed 2D Metallic Dielectric Photonic Crystals (MDPhC) fabricated on 6” Si wafer has properties of solar broadband, omnidirectional and tunable selective absorption as well as long-term thermal stability as

shown in Fig. 1.1. The broadband absorption is due to the high density of cavity modes supported by nanocavity structures that light with various wavelengths can couple with.

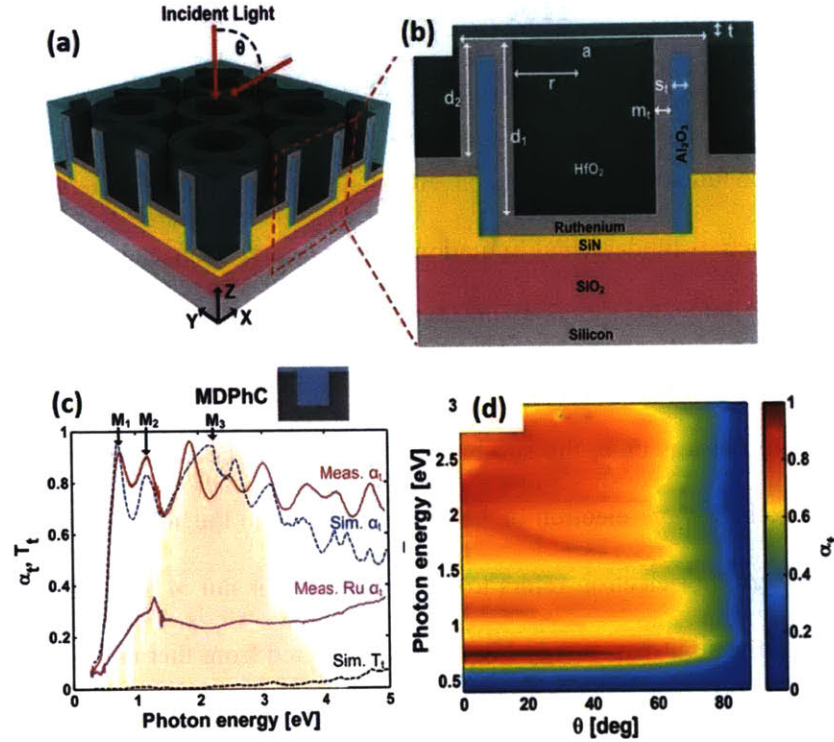


Fig. 1.1 (a) and (b) Schematic diagram of the Metal-Dielectric Photonic Crystals (MDPhC) structure. (c) The total measured and simulated absorption spectrum for MDPHC. (d) Contour plot of the RCWA simulated absorption spectrum as a function of incident angle θ . [6]

Be inspired by MDPHC, we came up with a new design of Metallic-Semiconductor Photonic Crystals (MSPhC) to take advantage of broadband absorption, and then generate hot electrons subsequently, showing the potential of large-scale, low-cost and efficient solar energy conversion. MSPhC has similar nanocavities structure but changing the materials to metal and n-type semiconductor. Metal acts as an active layer of hot electrons generation via interband or intraband transition after absorbing light. N-type semiconductor is used to form schottky interface with metal, creating internal electric

field to collect injected hot electrons.

This thesis starts from brief introduction of the background knowledge of photonic crystals and hot electrons. Then simulation and experimental methods are mentioned. After that, results of simulation and experiments are shown and discussed. This thesis research firstly focuses on optical simulation of MSpC. General optical properties of MSpC have been studied to confirm its good absorption performance. Detail analysis includes structural parameter dependence, absorption analysis, and mode analysis. Besides simulation, MSpC has been fabricated as well with wafer scalable microfabrication techniques. And its electric and photo-electric properties have been tested preliminarily.

Chapter 2 Theoretical Background

2.1 Photonic Crystals

Photonic crystals are composed of materials with periodic dielectric functions that affect the propagation of electromagnetic waves in a similar way as the periodic potential in a crystal lattice affects the electron motion. Photonic crystals contain repeating regions of high and low dielectric constant. Photons propagating through this structure or not depends on their wavelength. Wavelengths that are allowed to travel are known as modes and groups of allowed modes form bands. Photonic crystals with photonic bandgaps can be designed and constructed to prevent light of certain frequency from propagating in certain directions with certain frequencies, or to allow propagation in anomalous but useful way. Photonic crystals can reflect and trap light and thereby forming useful optical tools such as mirrors, waveguides, and resonant cavities [7]. Fig. 2.1 shows simple examples for one, two, and three dimensional (1D, 2D, 3D) photonic crystals that are periodic in one, two, and three directions respectively.

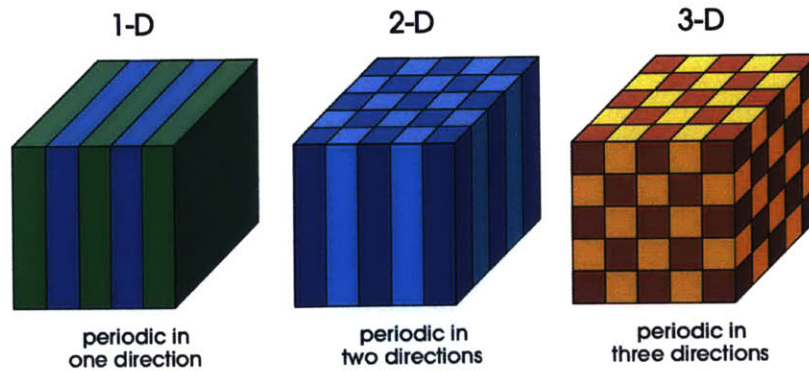


Fig. 2.1 Schematic diagram of simple examples for 1D, 2D, 3D photonic crystals. Different colors represent materials with different dielectric constants. [7]

Conventional photonic crystals are composed of low-loss materials which barely absorb light. And that is also the reason why metallic photonic crystals are usually used in microwave region since metal becomes lossy in visible region. In this thesis, the term photonic crystals is used in a broad way. The term Metallic-Semiconductor Photonic Crystals (MSPhC) is just used to describe the two dimensional periodic metallic-semiconductor nanocavities that can change propagation properties of photons. And MSPhC is actually used in the lossy region of metal such as visible region to absorb as much solar energy as possible.

2.2 Hot Electrons

Hot electrons refer to electrons that are not in thermal equilibrium with the atoms in a material. Its distribution can be fundamentally described by the Fermi function with an elevated effective temperature [8]. Hot electrons can exist in various kinds of material. In this research, hot electrons in metal have been focused on.

Photoelectric hot electrons generation is the process that when a photon with sufficient energy strikes the metal, the energy from the photon can be transferred and excites electron to a higher available energy level above Fermi level via interband or intraband transition as shown in the left part of Fig. 2.2. If the generated hot electron has sufficient kinetic energy to overcome the potential barriers necessary for breaking an interface state, hot electrons injection can happen. An efficient mechanism for capturing such hot electrons is to form a Schottky barrier with an appropriate semiconductor. Fig. 2.2 shows a Schottky barrier between a metal and an n-type semiconductor, such as TiO₂. TiO₂ is a good electron-accepting metal oxide due to the high density of states (DOS) in its conduction band, which permits fast electron injection. Hot electrons with energies

higher than the Schottky barrier energy ϕ_{SB} can be injected into the semiconductor. Tunneling across the barrier can also take place with a much lower probability. The energy barrier (ϕ_{SB}) for hot electrons to overcome in this system is considerably smaller than the bandgap of the semiconductor (E_g) [9][10]. Therefore, this photoelectric hot electron generation and injection phenomena opens a new horizon of solar energy conversion.

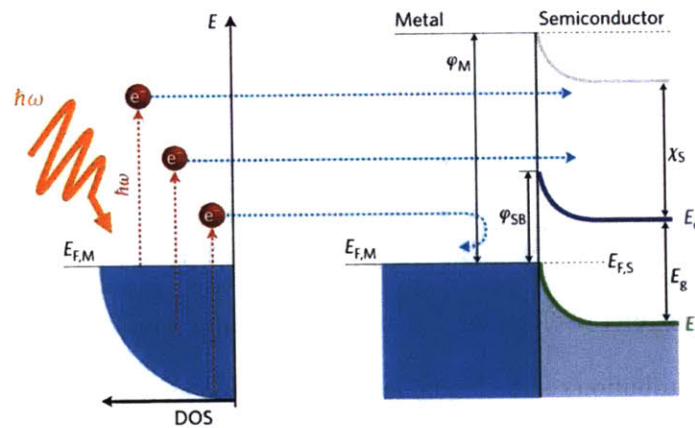


Fig. 2.2 Hot electrons can be injected into a semiconductor by forming a Schottky barrier with the plasmonic nanostructure. Hot electrons with energies high enough to overcome the Schottky barrier $\phi_{SB} = \phi_M - \chi_S$ are injected into the conduction band E_c of the neighboring semiconductor, where ϕ_M and χ_S are the metal work function and the semiconductor electron affinity. [11]

Chapter 3 Device Design

3.1 Structure Design

Previous study in our group showed that the designed 2D MDPPhC fabricated on 6" Si wafer has properties of solar broadband, omnidirectional and tunable selective absorption as mentioned in Chapter 1. Be inspired by this study, MSPhC is designed to achieve solar broadband hot carrier generation. The cross sectional schematic diagram of designed MSPhC is shown in Fig. 3.1(a). Similar cavity structure is used to support various optical modes that can couple to light with various wavelength. Al_2O_3 cavity shell on top of Si/SiO₂ substrate first acts as a structural support. On top of Al_2O_3 , there is a layer for light absorption and hot carriers generation, which metal is used. Since the absorption of thin metal layer is dominated by allowed interband and intraband transition instead of being limited by the bandgap of the semiconductor, broadband absorption and subsequent hot carriers generation can be expected. Then the semiconductor layer in the structure is used to form a Schottky barrier with the metal, which creates internal electric field for hot electrons collection. The schematic of the absorption, carrier generation and collection process in the designed structure is shown in Fig. 3.1(b).

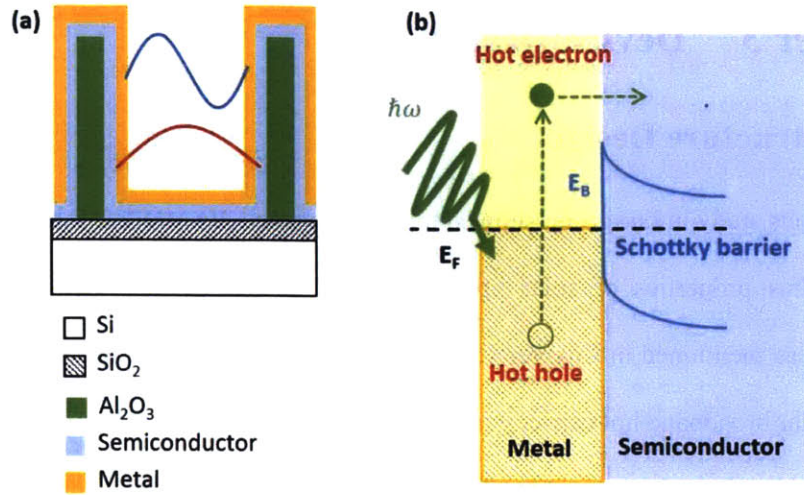


Fig. 3.1 Schematic diagram of (a) cross section of designed MSPhC, and (b) the process of subsequent light absorption, hot electron generation and collection.

3.2 Factors Affecting Hot Electrons Injection Efficiency

Not all hot electrons can have enough energy and not all hot electrons with enough energy are able to inject into semiconductor. There are factors that can affect hot electron collection efficiency and need to be taken into account for detail design. These factors will be discussed in following sections. The hot electron collection is broken into three parts: generation, transport, and injection. The results indicate that thin metal is more ideal for hot electron collection.

3.2.1 Generation: Band Structure and Density of States

Photoelectric hot electrons generation in metal can happen through interband and intraband transitions. This indicates that the band structure and density of states of metal significantly affect the generation efficiency and energy distribution of hot electrons. In general band diagram, intraband transition is less likely to happen, since the momentum

required for momentum conservation is much larger than electron or plasmon momentum according to Lindhard function. However, in metal nanostructure such as thin film or nanoparticle, momentum conservation no longer needs to be satisfied due to broken symmetry and quantum confinement in one direction at least. It implies metal nanostructure is preferred for enabling intraband transition [12]. After absorption, the energy and momentum of excited hot electrons are distributed according to the density of initial and final states in the metal. The hot electron may have an energy above the Fermi energy ranging from zero up to the photon energy absorbed. Its probability distribution depends on the detailed band structure. In free electron model, the density of state $g(E)$ is proportional to the square root of energy as shown in Fig. 3.2. Hot electron can have energy distributed from E_F to $E_F + \hbar\omega$ where $\hbar\omega$ is photon energy. Within that region, blue line shaded area represents hot electrons with sufficient energy to across schottky barrier φ_{SB} , excited from orange line shaded area. Therefore, it is indicated that high density of states near Fermi energy is ideal for obtaining larger fraction of hot electrons with enough energy for injection.

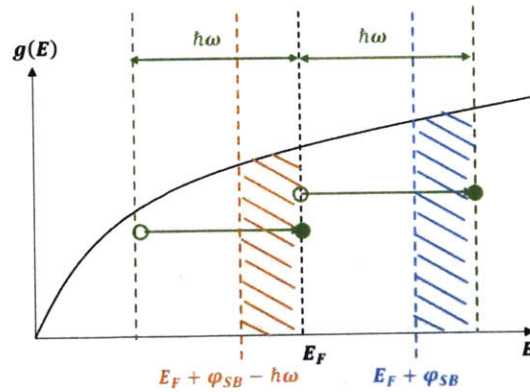


Fig. 3.2 Density of state for free electron model. Hot electron excited from $E_F - \hbar\omega$ to E_F can have energy distributed from E_F to $E_F + \hbar\omega$. Within it, hot electron in blue line shaded area (excited from orange line shaded area) have sufficient energy to across schottky barrier.

3.2.2 Transport: Mean free path

Relaxation of electrons with a non-Fermi distribution in metal nanostructures occurs through electron–electron (<100fs), electron–phonon (1–10ps) and phonon–phonon (~100ps) interactions. Hot electron injection then has to occur before or during thermalization as a result of electron–electron interaction [11]. Theoretical mean free path (MFP) of electron-electron scattering for metals are around 10-60nm [13][14]. Which means the metal layer thickness should not exceed the MFP to have effective hot electron injection. Otherwise, most of generated hot electrons thermalize before injection.

3.2.3 Injection: Electron Momentum

In a simple model, hot electrons are expected to generate isotropically with momentum k in random direction. The probability of injecting into the semiconductor depends on both the hot electron energy and the component of momentum normal to the interface, which first proposed by Fowler [15] to best describe the experimental energy dependence of the photoemission yield. Besides energy criteria, the component of electron momentum normal to the surface k_z must be high enough to overcome the critical momentum k_{crit} depended on barrier energy. This leads to an effective cone in k space with allowed momenta for injection as shown in Fig. 3.3. The critical momentum k_{crit} defines an effective angle of hot electron injection,

$$\theta_{eff} = \cos^{-1} \frac{k_{crit}}{k} = \cos^{-1} \frac{\sqrt{E_F + \varphi_{SB}}}{\sqrt{E_{ele}}} \quad (2.1)$$

For internal photoemission, the hot electron energy E_{ele} is typically close to $E_F + \varphi_{SB}$, defining a rather small angle. This effective angle of injection analysis assumes a perfect, planar interface. For a rough interface, the escape cone may be larger and the normal momentum constraint relaxed. As a best-case scenario, one could consider that all hot

carriers reaching the interface with sufficient energy can escape regardless of momentum direction. Also accounting for specular reflection of a hot carrier at the back surface of a thin film.

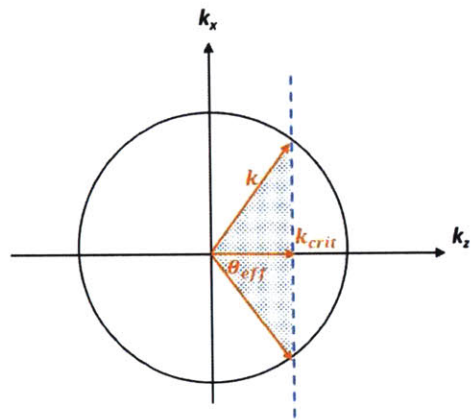


Fig. 3.3 Schematic diagram of the effective cone for hot electron injection in k space.

Chapter 4 Optical Simulation

4.1 Finite-difference Time-domain (FDTD) Simulation

With preliminary design of MSPhC, the optical simulation of modeling the interaction between light and MSPhC is conducted. The results can provide profound understanding of the structure and the direction of optimization. Finite-difference Time-domain (FDTD) technique is used for simulation. A brief introduction and the advantage of using FDTD is elaborated as following.

4.1.1 FDTD Models and Methods

FDTD is a numerical analysis technique used for modeling computational electrodynamics, finding approximate solutions to the associated system of differential equations. The FDTD method belongs in the general class of grid-based differential numerical modeling methods. The time-dependent Maxwell's equations are discretized using central-difference approximations to the space and time partial derivatives. The resulting finite-difference equations are solved in a leapfrog manner: the electric field vector components in a volume of space are solved at a given instant in time; then the magnetic field vector components in the same spatial volume are solved at the next instant in time; and the process is repeated until the desired transient or steady-state electromagnetic field behavior is fully evolved.

From Maxwell's differential equations, the change in the E-field in time is dependent on the change in the H-field across space. This results in the basic FDTD time-stepping relation that, at any point in space, the updated value of the E-field in time is dependent on the stored value of the E-field and the numerical curl of the local distribution of the H-field in space [16]. The H-field is time-stepped in a similar manner. Iterating the E-field

and H-field updates results in a marching-in-time process wherein sampled-data analogs of the continuous electromagnetic waves under consideration propagate in a numerical grid stored in the computer memory. This description holds true for 1-D, 2-D, and 3-D FDTD techniques.

To implement an FDTD solution of Maxwell's equations, a computational domain must first be established, it is the physical region over which the simulation will be performed. The E and H fields are determined at every point in space within that computational domain. The material of each cell within the computational domain must be specified. Any material can be used as long as the permeability, permittivity, and conductivity are specified. Once the computational domain and the grid materials are established, a source is specified. The source can be current on a wire, applied electric field or impinging plane wave. In the last case FDTD can be used to simulate light scattering from arbitrary shaped objects, planar periodic structures at various incident angles [17][18], and photonic band structure of infinite periodic structures [19][20]. Since the E and H fields are determined directly, the output of the simulation is usually the E or H field at a point or a series of points within the computational domain. The simulation evolves the E and H fields forward in time.

4.1.2 Strength of FDTD

Many of the strength of FDTD make it ideal for simulating MSpHC. First of all, FDTD is a time-domain technique, when a broadband source is used, the response of the system over a wide frequency range can be obtained with a single simulation. This is useful in applications where resonant frequencies are not exactly known, or anytime that a broadband result is desired. Second, since FDTD calculates the E and H fields everywhere in the computational domain as they evolve in time, it can provide animated

displays of the electromagnetic field movement through the model. It helps understanding real time interaction in the model. Also, FDTD technique allows user to specify the material at all points within the computational domain. A wide variety of linear and nonlinear materials can be naturally and easily modeled. All of these strengths are ideal for simulating the interaction between sunlight and the MSPhC, since a broadband result is expected and the ability of easily varying materials can be a great advantage.

4.2 FDTD Simulation of MSPhC

By running FDTD simulation, the optical properties of MSPhC can be studied. One of the interesting and relatively straightforward properties is reflection, transmission, and absorption (RTA) spectrum. A commercial software Lumerical is used for FDTD simulation. Within Lumerical, we can construct 3D unit structure, assign materials, set boundary conditions, and place 2D intensity monitors at top and bottom of the structure to collect reflected and transmitted light intensity. Monitors can also be placed inside the structure to collect values of electric and magnetic field or dielectric constants. By further introducing the broadband plane wave source from 200nm to 2 μ m, RTA spectrum can be obtained as shown in Fig. 4.1, assuming incident light has intensity 1 at each wavelength. Within RTA spectrum, absorption spectrum is the one with most interest since it gives the amount of photon energy transfer which can potentially lead to hot carrier generation. The simulation shows that MSPhC has a broad absorption range up to about 1.5 μ m, covering the main region of solar radiation.

In following sections, the absorption behavior of MSPhC with various structural parameters has been studied. Optical mode analysis is also done to understand how light interacts with MSPhC nanostructure.

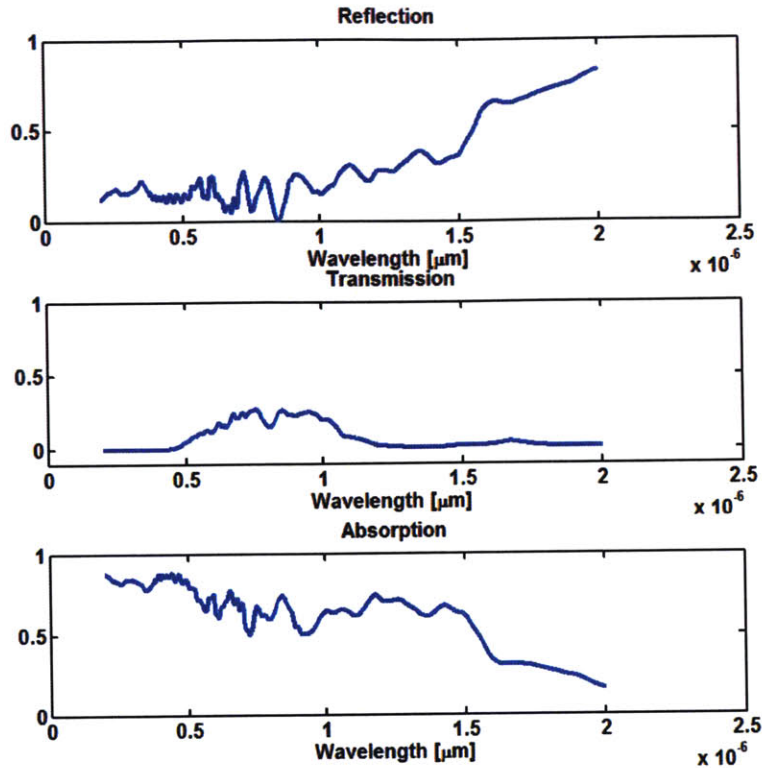


Fig. 4.1 Reflection, transmission, and absorption (RTA) spectrum of MSPhC (Structure parameters are chose base on experimental values: cavity radius: 320nm, periodicity: 840nm, depth: 1 μ m, Au layer: 13nm, TiO₂: 75nm, Al₂O₃: 50nm)

4.3 Structural Parameters Dependence

The broad absorption of MSPhC is thought to be contributed by various optical modes supported by the unique nanostructure. Detail mode analysis will be discussed in following section. One of the basic mode, cavity mode, is focused in this section. Metal cavity acts as a potential well to photons with wavelength in the lossy region of metal. Which indicates that light with wavelength satisfied standing wave conditions of the cavity can couple to those standing wave modes, here we call it cavity modes, and be trapped. Long interaction time of trapped light and metal then significantly increases

metal absorption. The structural detail of cavity can significantly affect coupling conditions and then absorption behavior. The absorption spectra of MSPhC under different structural parameters are simulated to understand how each parameter affects absorption and to find optimal structural design. Parameters that have been tuned include dimensional parameters, radius, depth, periodicity of cavities, and thicknesses of each materials Al_2O_3 , TiO_2 and Au. Each parameter is swept over a reasonable region while every other parameters stay the same. Fig. 4.2 and Fig. 4.3 show resulted absorption dependence. Each data point represents total absorption under one parameter set calculated by integrating the correlated absorption spectrum and dividing with source power. Since absorption spectrum can change its shape and peak positions under various parameters, solar-weighted total absorption is also calculated by considering light source which is not identical at every wavelength but has relation as solar radiation spectrum. Non-solar-weighted total absorption gives general absorption performance of MSPhC through 200nm to $2\mu\text{m}$, while solar-weighted total absorption gives more information when considering solar application.

First, the radius dependent absorption is simulated. A trade-off between number of cavity modes and light trapping are expected, since cavity with larger radius can support more modes but lose the degree of confinement at the same time. Fig. 4.2(a) shows that maximal absorption of MSPhC happens at radius $r \sim 500\text{nm}$ for non-solar weighted and $r \sim 250\text{nm}$ for solar-weighted cases. For depth dependence, deeper cavity are expected to support more cavity modes and increase absorption. Results in Fig. 4.2(b) agrees with the tendency that total absorption increases with cavity depth d . Periodicity dependence in Fig. 4.2(c) shows smaller change of absorption compare to first two plots. Changing periodicity is a more complicated situation. Larger periodicity gives rise of gap modes, which means light can couple to the gaps between cavities, leading to increasing

absorption in long wavelength region. However, more diffraction can happen with larger periodicity since cavity array can look like grating to light with wavelength smaller or close to cavity periodicity. Results of simulated dimensional parameter dependent absorption mostly agree with our qualitative intuition, and give us guidance for fabricating the working MSpC device.

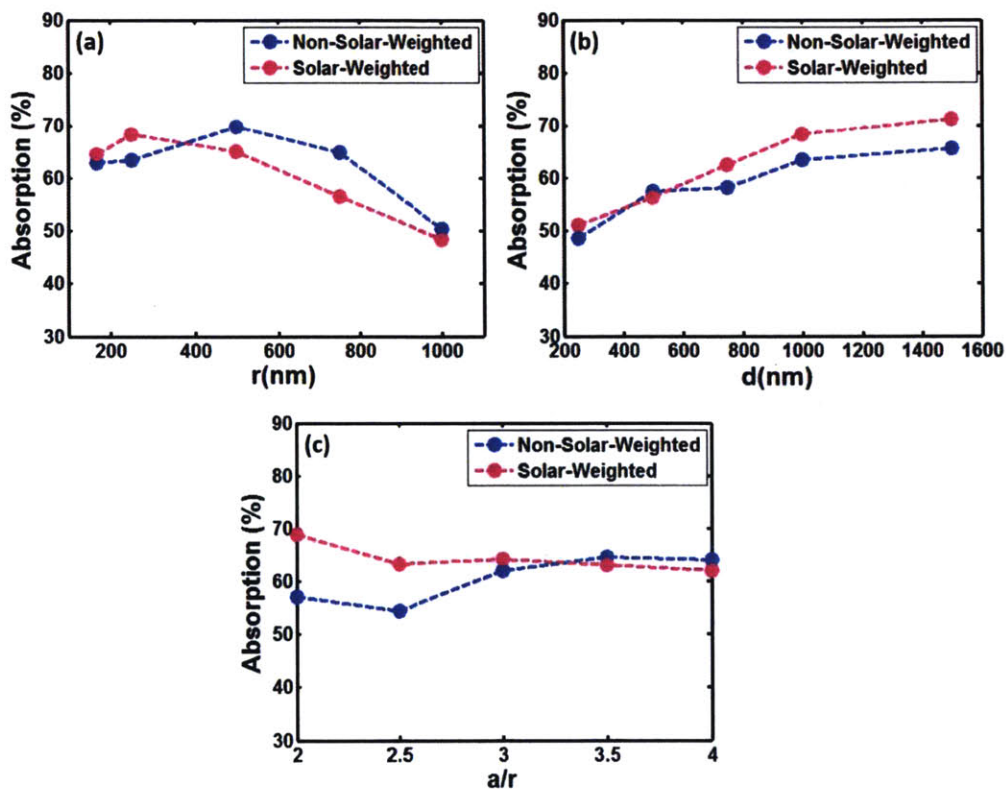


Fig. 4.2 Simulated (a) Cavity radius r , (b) Cavity depth d , and (c) Cavity periodicity a dependent total absorption. Where r is varied from 167 to 1000nm, d is varied from 250 to 1500 nm, and a is varied from $2r$ to $4r$.

In Fig. 4.3(a) and (b), the thickness of Al₂O₃ and TiO₂ are changed in the range around 20nm to 100nm. The resulted absorption didn't change much. Which is because

although with thinner Al₂O₃ or TiO₂, which means thinner side wall, gap mode can exist, it is in long wavelength region and the gap won't change much in the tuning length scale. Therefore the total absorption is not significantly affected. In Fig. 4.3(c), Au thickness is changed from 5 to 105 nm. The absorption dramatically decrease with increasing Au thickness. This is an interesting results since Au is considered as the absorbing layer. The simulation shows that thinner Au actually gives higher total absorption. However, note that the simulation shows the absorption of whole MSPhC structure. It is not clear which materials contributes total absorption. Before making further statement, absorption contribution analysis is conducted in next chapter.

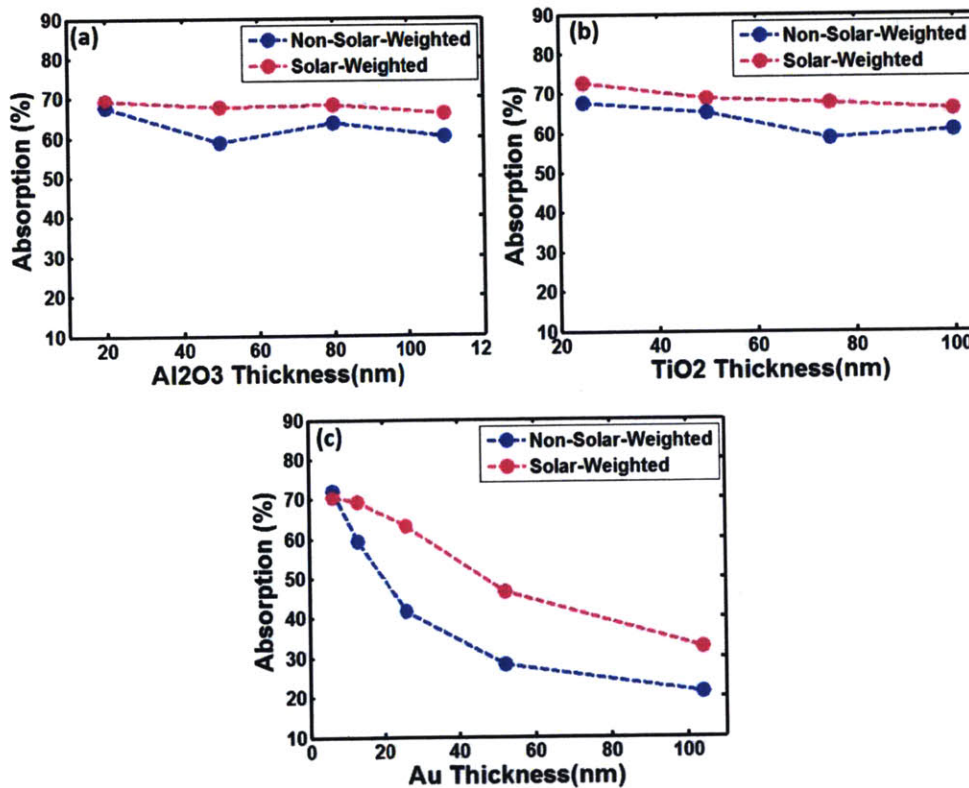


Fig. 4.3 Simulated (a) Al₂O₃, (b) TiO₂, and (c) Au thickness dependent total absorption.

4.4 Absorption Contribution Analysis

Besides simulating total absorption spectra, the amount of contribution to total absorption of different materials in the whole structure are also analyzed. By classical electrodynamics, the spatial power absorption is given by the divergence of the Poynting vector which by Maxwell's equations can be written as [21]-[24]

$$P_{abs} = -\frac{1}{2}Re[-\nabla \cdot S] = -\frac{1}{2}\omega Im[\epsilon]|E|^2 \quad (4.1)$$

Where S represents poynting vector, ω is frequency of light, $Im(\epsilon)$ is the imaginary part of permittivity of material where light propagating with in, and $|E|$ is the magnitude of electric field. By collecting electric field values at each position point in simulated structure from FDTD simulation, and by having permittivity data of each material, the spatial power absorption at each position can be calculated.

Fig. 4.4 shows the simulated electric field intensity image at incident wavelength of 752nm, and the image of calculated spatial power absorption. The brightness represents intensity of $|E|$ and P_{abs} respectively. Note that the shape of cavity is made to be parabolic instead of straight wall base on real structure from fabricated device we saw via SEM. The color difference in Fig. 4.4(b) is in log scale, indicating that Au dominates the absorption of whole structure where the amount of absorption in Au is ~ 3 to 5 orders higher than other materials. In order to represent absorption contribution more quantitatively, we sum up all the P_{abs} in each material, which represents total absorption happened in it, and then do it under various wavelength from 200nm to 2 μ m. With this analysis method, we can now decompose the original absorption layer to contribution of each materials. Fig. 4.5 shows spectra of the ratio of absorption contribution and total absorption of each materials in MSPhC. It implies that Au is the dominant absorbing material in MSPhC which is ideal for hot electron generation purpose.

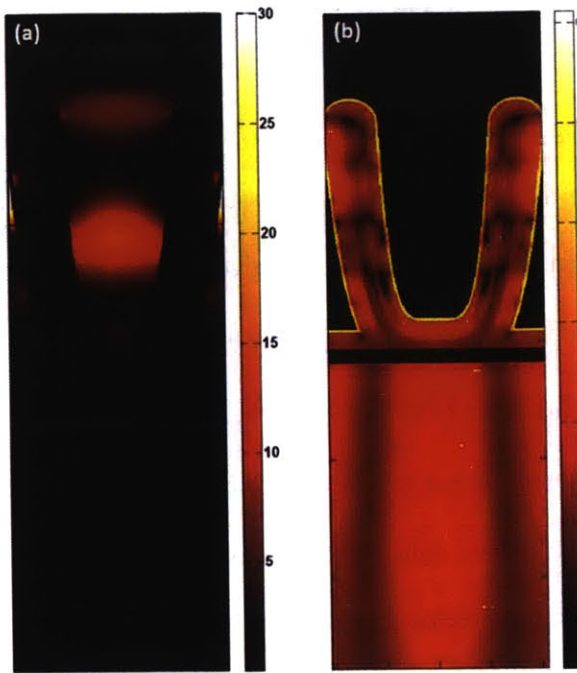


Fig. 4.4 Simulated images of (a) electric field intensity and (b) special power absorption, at incident wavelength of 752 nm.

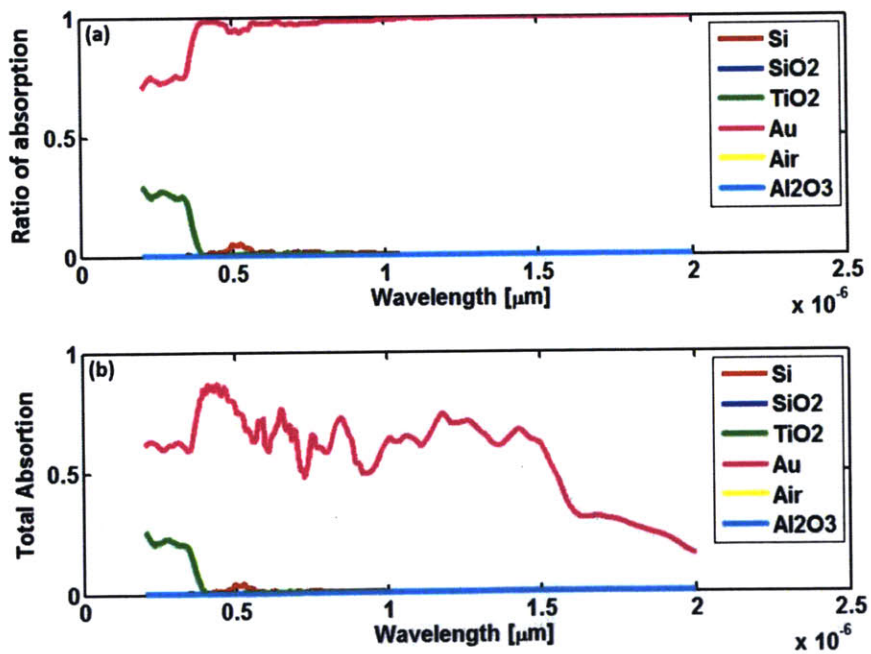


Fig. 4.5 Simulated spectra of (a) ratio of absorption contribution, and (b) total absorption of each materials in MSPhC

The amount of Au and TiO₂ absorption under different Au thickness are also calculated and shown in Fig. 4.6. The absorption of TiO₂ decreased while Au thickness increasing. The absorption of Au shows similar trend that thinner Au gives higher absorption with peak value at thickness ~5nm. The possible reason of this result is that thinner Au film enables light to penetrate through it and couple into various optical modes supported by whole structure. Increasing interaction time of light and Au then leads to increased absorption. While with thick Au film, light cannot penetrate through it and thus most of light cannot couple to the structure. It also explains the decreasing TiO₂ absorption with thick Au. In this case, Au shows more bulk-like optical property which is reflective in long wavelength region. In summary, the absorption contribution analysis shows that from optical point of view, thinner Au is preferred for high absorption.

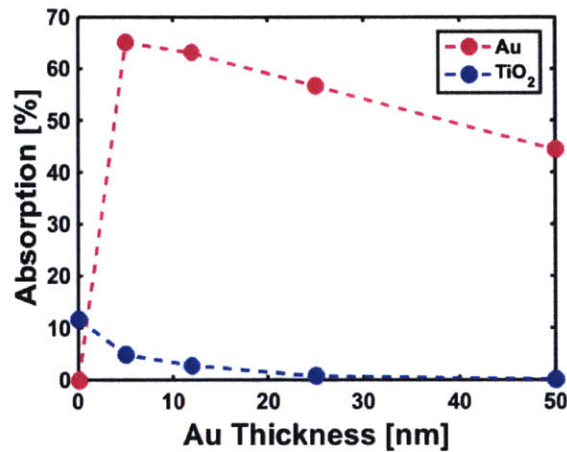


Fig. 4.6 FDTD simulated absorption in both Au and TiO₂ as a function of Au thickness.

4.5 Modes Analysis

By looking at MSPhC, intuitively and qualitatively thinking, it can possibly support 4 kinds of optical modes as shown in Fig. 4.7. First one is cavity mode, coupling light

inside cavity and the resonant wavelength depends on cavity dimensions. Second is gap mode, which is similar to cavity mode. Light can couple in the gap between two cavities and the resonant wavelength depends on gap dimensions. The third one is waveguide mode. Since cavity wall forms a metal/insulator/metal (MIM) structure, light can couple in insulating layer ($\text{Al}_2\text{O}_3+\text{TiO}_2$) like it does in MIM waveguides [25][26]. The resonant wavelength of waveguide modes depend on permittivity of metal and insulator, and the insulator thickness. The fourth one is surface plasmon mode that can happen at metal/insulator interface, in here means Au/ TiO_2 interface. The resonant frequency depends on permittivity of metal and insulator. MSPhC can also supports other complicated modes mixed from these 4 basic kinds of mode.

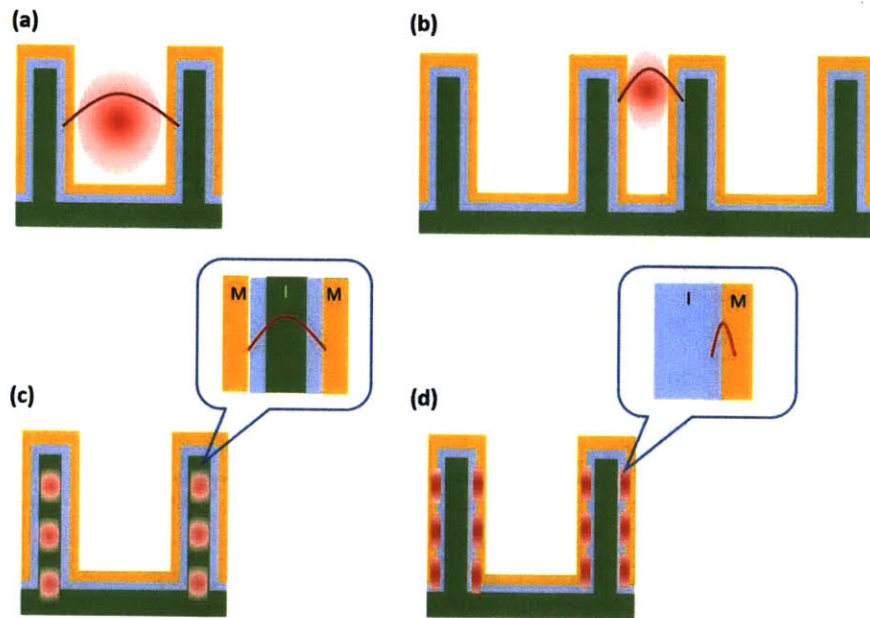


Fig. 4.7 Optical modes that MSPhC can possibly support: (a) cavity mode, (b) gap mode, (c) waveguide mode, (d) surface plasmon mode. Red figures represent electric field intensity of coupled light.

In order to do further mode analysis of the structure and to be more quantitative, another simulation method is used. For simulations in previous sections, broad band plane wave source is used, and 2D monitors are placed on top of and beneath MSPhC to measure reflection and transmission at different wavelength. To do mode analysis, dipole sources and time monitors are used. Fig. 4.8 shows the simulation unit for mode analysis. 10 broad band dipole sources are randomly positioned in the structure to provide impulses, exciting all possible modes. 8 1D time monitors are also randomly placed to collect amplitude signals versus time. Then by applying Fourier transformation, figures of amplitude versus frequency (wavelength) can be obtained. Any characteristic peak appears on the figure indicating one of the possible mode that MSPhC supports.

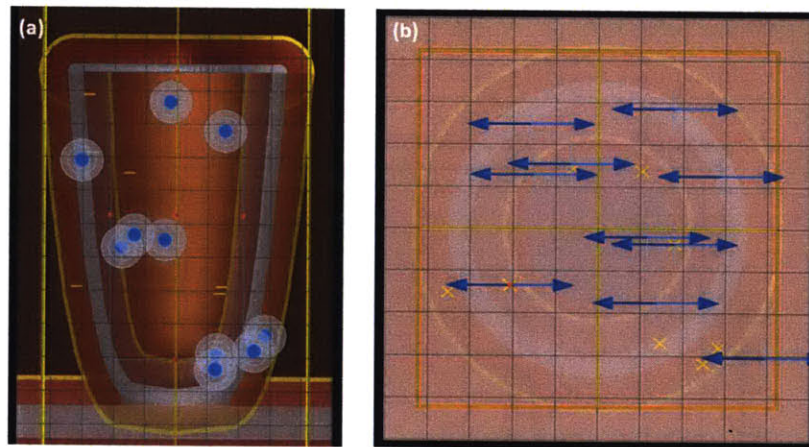


Fig. 4.8 (a) Cross sectional diagram and (b) top view of simulation unit with 10 randomly positioned broad band dipole sources with polarization out of plane (blue dots and arrows), and 8 1D time monitors (yellow lines).

Fig. 4.9 shows the results by sum up through all time monitors with Au film thickness of 13, 26, and 52nm. Thickness dependence follows the tendency we found in previous section that thinner Au film gives higher magnitude. The first mode at around

500nm is a dominant mode and its field intensity image is shown in Fig. 4.10(a), which look like a waveguide mode existing in the sidewall of MSPhC. The second mode is around 600nm with smaller peak. The corresponding field intensity image in Fig. 4.10(b) shows a surface plasmon mode that light propagates along Au/air and Au/TiO₂ interfaces. Note that surface plasmon mode has larger full width at half max value (FWHM) indicating that it is a higher loss mode. The higher loss is due to the peak E-field of surface plasmon mode locates in the metal where absorption is high. Cavity mode (Fig. 4.10(c)) is also observed in longer wavelength region at around 700nm, but the corresponding amplitude are several orders of magnitude below first two modes. Here we demonstrate a way to do mode analysis of MSPhC. The preliminary results are still under studying and further improvement. Recently, we are trying to use plane wave source for mode analysis since it is closer to free space light input.

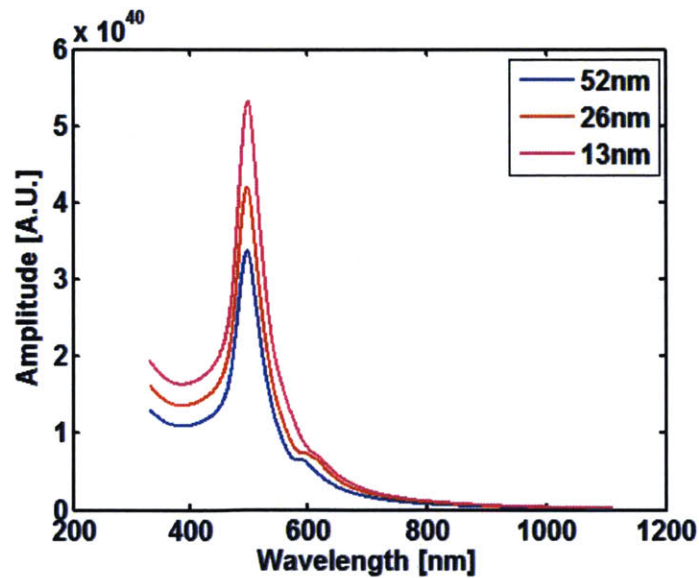


Fig. 4.9 Amplitude to wavelength figure by summing up all 8 time monitors with varying Au film thickness of 13, 26, 52nm.

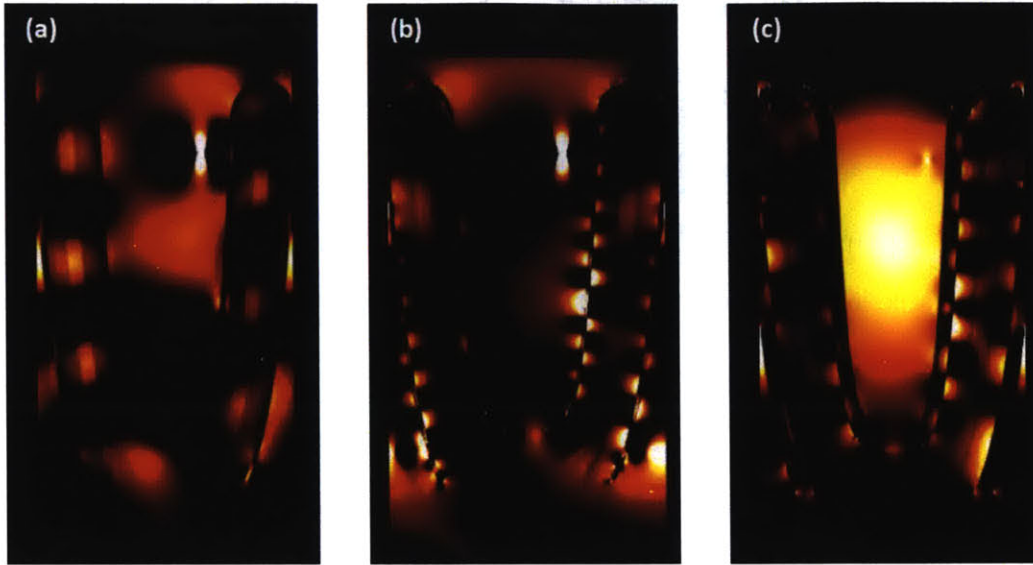


Fig. 4.10 Simulated E-field intensity image at (a) 500nm, (b) 600nm, and (c) 700nm. Which corresponds to waveguide mode, surface plasmon mode, and cavity mode.

Chapter 5 Preliminary Experimental Results

MSPhC are fabricated with microfabrication techniques developed for MDPHC. From the simulation results, we got the sense of how to choose cavity dimensions to maximize absorption. The resolution limit of the optical stepper we used is 600nm, and the smallest periodicity a obtainable is 800nm. Addition with non-idealness of fabrication, the MSPhC we fabricated has parameters of cavity radius $r \sim 320\text{nm}$, periodicity $a \sim 840\text{nm}$, and depth $d \sim 1\mu\text{m}$. The fabrication process and images of MSPhC devices and preliminary measurement results are shown and discussed in the following sections.

5.1 Fabrication Process

5.1.1 Nanocavity Array

The fabrication process of MSPhC is shown in Fig. 5.1(a)-(e). It begins on a 6" silicon wafer cleaned with the RCA clean process. 100nm of thermal oxide is then deposited on the wafer followed by 1 μm of sacrificial Poly Si via low pressure chemical vapor deposition (LPCVD). The thickness of Poly Si directly relates to the depth of cavities. Poly Si is patterned via an optical stepper with center wavelength of 369 nm. The photo-mask consists of a square checkerboard pattern with square dimensions of 0.6 $\mu\text{m} \times 0.6 \mu\text{m}$. Due to the resolution limit of the stepper, the square pattern resolved to circles on the developed photoresist with a minimum inter-circle spacing of 200 nm. The Poly Si layer is then etched via an SF₆ based RIE etch as shown in Fig. 5.1(b). To remove any undesired debris on the surface, the photoresist is then removed via an ashing process, followed by a piranha and RCA clean. In Fig. 5.1(c), 50 nm of Al₂O₃ is conformally deposited via atomic layer deposition (ALD) and anisotropically etched via a Cl₂ + BCl₃ based reactive ion etch (RIE) leaving only the sidewalls left. In Fig. 5.1(e), a XeF₂ gas

phased etch is used to etch the Poly Si only, thus leaving free-standing Al_2O_3 cylindrical shells on the wafer surface [27]-[29].

5.1.2 Metal and Semiconductor Layers

Fabricated nanocavity array with Al_2O_3 sidewall structural support can then be used as a base substrate on which we can deposited desired semiconductor and metal layers via various deposition process. Fig. 5.1(f)-(h) show the deposition of materials that have been first chosen, TiO_2 and Au. Approximately 75 nm of TiO_2 is deposited via ALD over the Al_2O_3 shells followed by post annealing under 450°C , in air for 1 hour. About 13nm of Au then deposited on TiO_2 via DC sputtering. Thick ($\sim 100\text{nm}$) Au and Ti are also deposited at two sides of chip as contact electrodes, where Ti forms an ohmic contact with TiO_2 .

In our new design of device up to date, which will be mentioned in Chapter 5, ITO back contact ($\sim 30\text{nm}$) and Al_2O_3 interface passivation layer ($\sim 1\text{nm}$) are also deposited by sputtering and ALD to improve electric properties. Post annealing has performed on ITO under 415°C , in air for 2 hours.

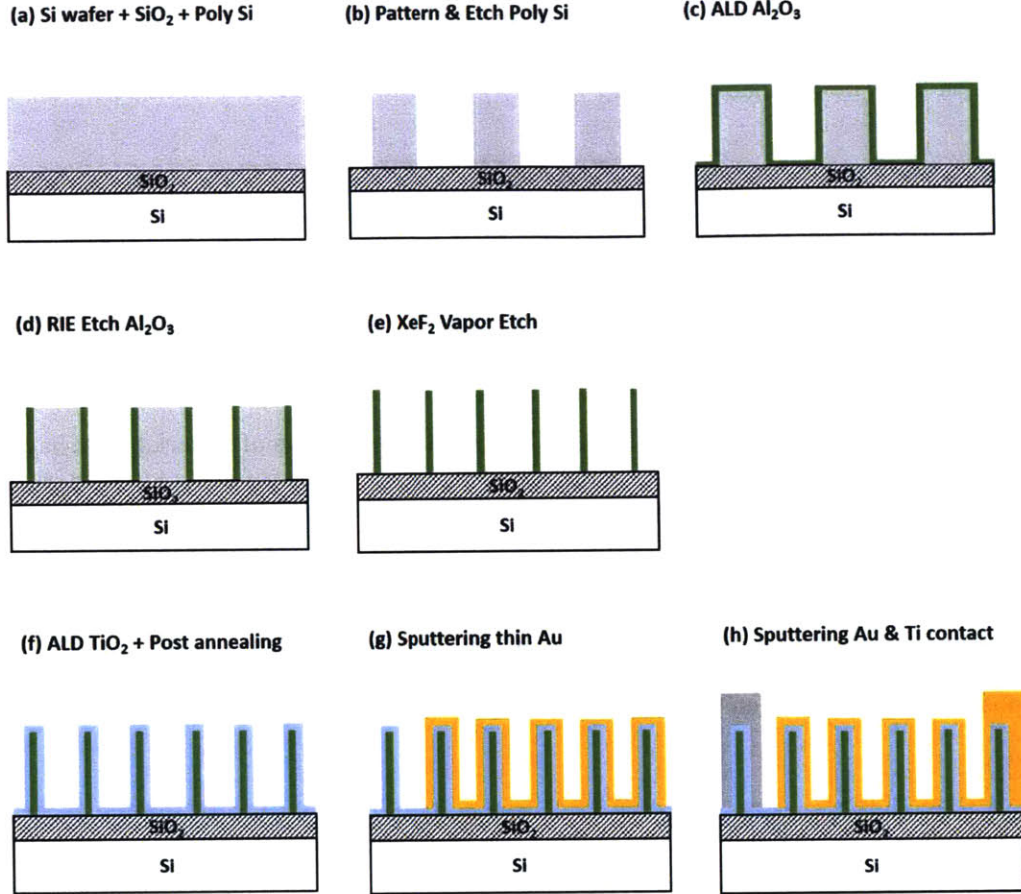


Fig. 5.1 Schematic diagram of wafer-scale MSpHC fabrication process.

5.2 Device Characterization Methods

5.2.1 Imaging

Top view and tilted Scanning Electron Microscopy (SEM) images are performed via Zeiss Supra 40 and Zeiss Ultra 55 with inlens detector and 5kV or 10kV accelerating voltage. Cross section images are done by JEOL JIB-4500 Focused Ion Beam (FIB) system.

5.2.2 I-V curve and Photoresponse

Keithley 2400 Digital Source Meter and a probe station are used for I-V measurement. Wavelength dependent photoresponse is also been done by integrating the same system with additional optical set up. The photocurrent was directly measured via Keithley 2400 upon illumination with a 300 W Xenon arc lamp source monochromated by a holographic diffraction grating. To obtain more accurate photoresponse measurements, we used laser diodes at a few selected wavelengths from 405 nm to 850 nm. Due to high series/shunt resistance and surface area variations, each photoresponse measurement was normalized by the overall series resistance.

5.3 Images of Fabricated Device

Fig. 5.2(a) first shows the SEM image of fabricated Al_2O_3 shells, with depth $\sim 1\mu\text{m}$, radius $\sim 320\text{nm}$, and period $\sim 840\text{nm}$. The walls of cylindrical shells are actually parabolic than straight, which is due to non-ideal RIE etching which can be further corrected with process tuning. The top and cross sectional (milled by FIB) SEM images of fully fabricated MSpHC device with TiO_2 and Au layers deposited are shown in Fig. 5.2(b)-(c). It shows that junction materials cover Al_2O_3 cavities nicely and conformally. Fig. 5.2(d) is the photo image of 1cm by 1cm device cut from 6 inch wafer. The left side of the chip is just flat Au that has no cavities structure on it. The color difference between MSpHC device area and left side of chip indicates how periodic nanostructure changes absorption behaviors of thin Au film from reflective to significantly absorbing in visible region.

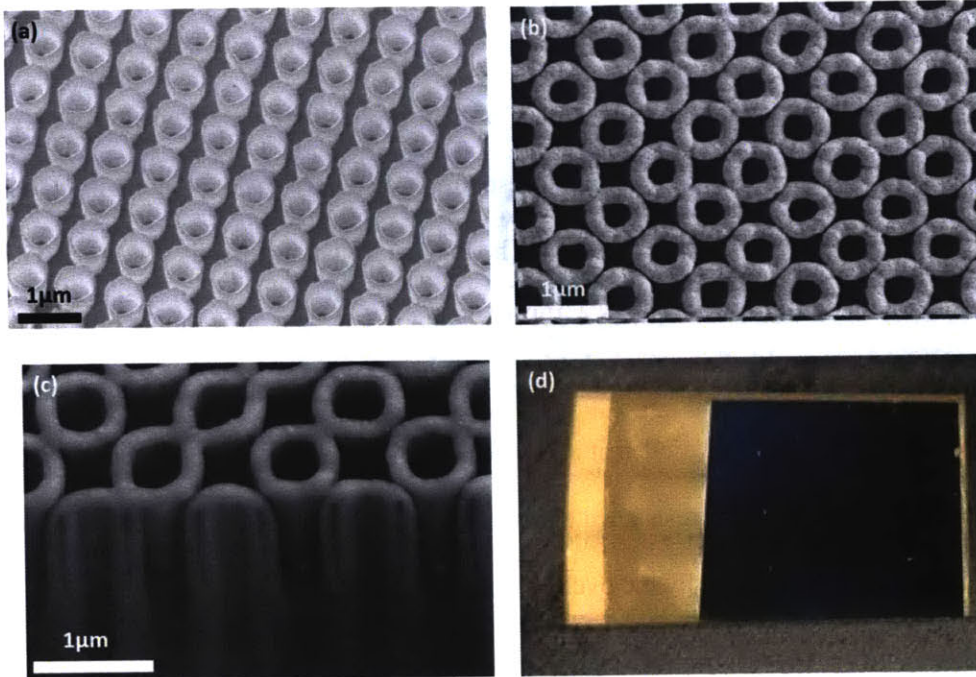


Fig. 5.2 (a) SEM image of Al_2O_3 shells. (b) Top view and (c) cross section view at 30° angle of fully fabricated device with TiO_2 and Au layers deposited. (d) Photo image of 1 cm by 1 cm device.

5.4 Reflection Spectrum

MSPhC is fabricated on Si wafer and Si absorbs light above its bandgap ($\sim 1.1\text{eV}$). Therefore, real absorption and transmission of the MSPhC is not measurable unless we fabricate the same structure on Quartz wafer which doesn't absorb visible light. Instead of absorption and transmission spectrum, we can still look at its reflection spectrum to see if there is any characteristic dip that may correspond to specific optical mode exist in MSPhC. Reflection spectra of devices are measured and shown in Fig. 5.3, where blue and red lines represent devices with and without $\sim 10\text{ nm}$ of Au film on it respectively. It shows that device with Au film on it has more dips compare to one has no Au film at wavelength of $\sim 500\text{nm}$ and $\sim 750\text{nm}$, indicating presence of resonant optical modes. However, the measured reflection spectrum did not match the simulation results shown

in Chapter 4 very well. The number of dips are not as many as expected. This inconsistency of simulated and experimental optical behavior is now under further study.

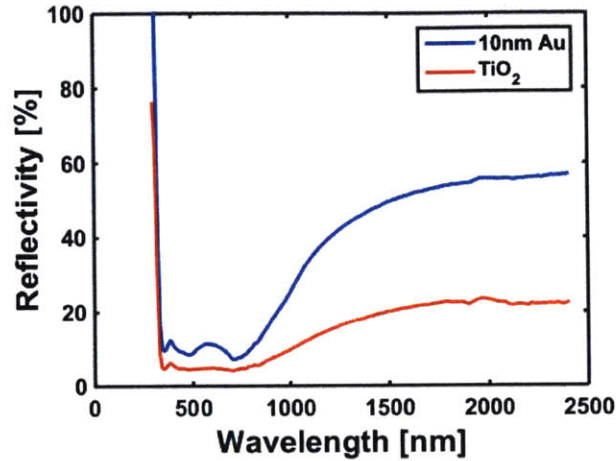


Fig. 5.3 UV-Vis reflection measurements at the 10 nm Au and TiO₂ surfaces on the MSPhC.

5.5 Diode Characteristics

Besides optical properties, electrical properties of MSPhC are also studied by first measuring its current to voltage behavior (I-V curve) as shown in Fig. 5.4(a). The resulted diode characteristics at the TiO₂/Au Schottky diode are quite poor, indicating significant leakage current and high series resistance exist in device. Works to improve the I-V behavior are ongoing, such as engineering TiO₂ thickness and annealing process, introducing passivation layer and back contact. One of the possible reason for leakage current is non ideal interface, where defect states at interface provide leakage paths for carriers in both direction and which have energy smaller than schottky barrier. In order to eliminate this kind of leakage current, introducing an ultra-thin oxide passivation layer is a common solution [30][31]. Therefore, ~ 1nm thick Al₂O₃ is deposited by ALD at the interface between TiO₂ and Au to passivate defect states while carriers with high enough

energy can still tunneling through it due to its ultra-thin thickness. The I-V curve of device with Al_2O_3 passivation layer is shown in Fig. 5.4(b). Rectifying performance is shown to be improved significantly that leakage current has been effectively eliminated. Note that the device with passivation layer however has much smaller current and becomes more sensitive to voltage which means that it can break down more easily under high applying voltage ($> 1\text{V}$). Recently, ITO back contact is also introduced to further improve carrier transport. By having ITO layer underlying TiO_2 , hot electron injected into TiO_2 can then transport via ITO to the collecting electrode. This path is much more conductive compared to the transport along TiO_2 , leading to smaller series resistance.

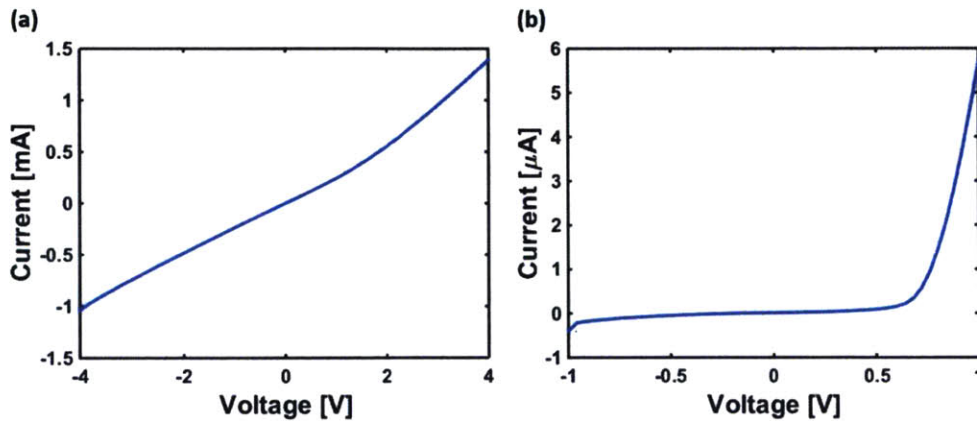


Fig. 5.4 Measured I-V curves of MSPhC (a) with and (b) without Al_2O_3 passivation layer at Au/ TiO_2 interface.

5.6 Wavelength Dependent Photoresponse

The measured high-resolution photoresponse data is shown in Fig. 5.5(a). The response is centered at 590 nm with a broad full-width at half-maximum (FWHM) of 235 nm. This response peak is located well below the band-gap of TiO_2 , which is approximately 400 nm, indicating sub-bandgap hot electron response. The peak position

also agrees well with the surface plasmon mode mentioned before in mode analysis. The first waveguide mode in the simulation was not experimentally observed in the photoresponse measurement. This could be either due to an inability to excite the first mode via free-space input, or that the waveguide mode does not contribute to hot electron current. Only plasmonic modes have been experimentally reported to contribute to hot electron current. As a result, it is not expected that cavity or waveguide modes should contribute to hot electron current. An explanation for the difference could be that plasmonic modes have a peak electric field at the metal/dielectric interface and contain plasmon oscillations of the free electrons in metal. Which might be preferred for hot electron generation. Fig. 5.5(b) shows the laser diode photoresponse of various measured nanostructured and flat devices. Laser source are used for obtaining more quantitative values of photoresponse. First, to demonstrate metal thickness variation effects, the photoresponse was measured on the same device after 3 incremental metal depositions from 10 nm to 30 nm. Note that the 10 nm thick Au layer device provided the highest photoresponse and broadest spectral absorption. This trend agrees with our simulations and theory shown in previous chapters that thinner metal layers would improve both optical and electrical energy conversion. For comparison, a flat chip with Au (30 nm)/TiO₂ (30 nm)/ITO (30 nm) is also shown. Our best measured device had no ITO with a layer profile of Au (10 nm)/TiO₂ (75 nm) and had a 12.28 factor increase compared to the flat chip at 639 nm. A major difference between the best measured device and the other devices is the TiO₂ film quality. Due to the shared facility use of our ALD tool, film quality was observed to vary widely, as a result we believe the best performing device was obtained because of the higher quality TiO₂ that was deposited. We are currently seeking alternative ALD to improve the film quality.

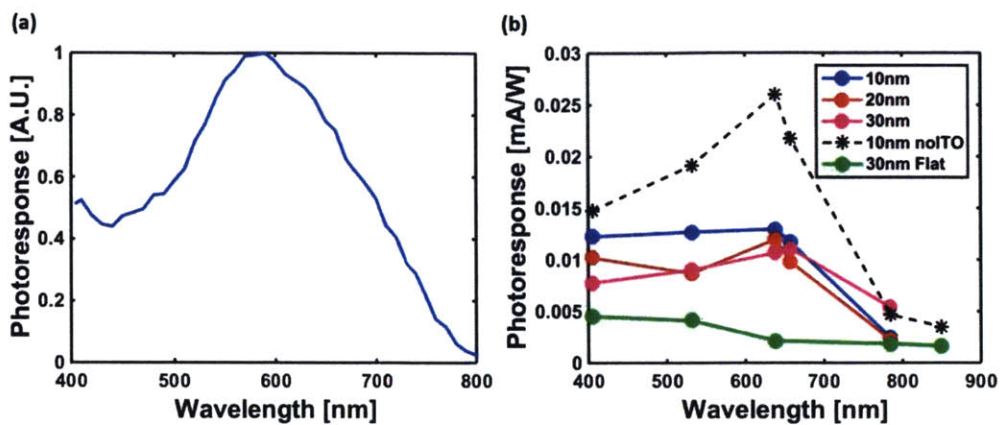


Fig. 5.5 (a) Measured high-resolution photoresponse of MSPhC. (b) Laser diode short-circuit photoresponse measurements at various Au thicknesses of 10 nm, 20 nm, and 30 nm. The black curve is our best reported device with no ITO layer. The green curve is a flat chip with identical films for comparison.

Chapter 6 Summary and Future Works

In this thesis, wafer-scale Metallic-Semiconductor Photonic Crystals (MSPhC) have been designed for photoelectric hot electrons generation. And both simulation and experiment of MSPhC have been done.

First, with FDTD optical simulation, the optical properties of MSPhC have been studied. The simulated absorption spectrum showed that MSPhC can achieve up to 70% absorption in a solar radiation range. Structural parameter dependent absorption gives a set of optimal cavity dimensions within the range of parameters that have been studied. Then absorption contribution analysis methods has also been developed to verify the amount of absorption of each materials in MSPhC. This enables us to study Au absorption behavior separately. The following Au thickness dependent absorption showed interesting Au thickness dependence that thinner Au gives higher absorption, and a peak value at thickness $\sim 5-10\text{nm}$. Since thinner Au film enables light to penetrate through it and couple into various optical modes supported by MSPhC. Mode analysis methods are also developed. By using multiple randomly placed dipole sources and time monitors, we can study various modes that MSPhC can support.

For experiment, MSPhC has been successfully fabricated with 6" wafer scalable microfabrication techniques, showing its potential of large-scale, low-cost fabrication process. Good schottky diode characteristics has been confirmed after further structure modification by introducing passivation layer and back contact. Measured wavelength dependent photoresponse shows peak located well below TiO₂ bandgap, indicating sub-bandgap hot electron response, 12 factors of photoresponse enhancement of MSPhC comparing to flat chip has also been observed.

This research is the begin of a project for Near Full-Spectrum Solar Water Splitting.

The designed MSpC showed that it can achieve broad solar absorption. For future works, we will try to convert those absorbed photon to collectable hot electron as much as possible and use those electrons to do water splitting. To achieve this goal, the most recent work is to improve film quality of both TiO₂ and Au by choosing different deposition tools or methods. P-type device is also under studying. By choosing different metal and p-type semiconductor, MSpC can also be used for hot-holes collection, which might be more efficient depending on hot carrier energy distribution. More complete and deeper mode analysis of MSpC is needed as well in order to get profound understanding of the mechanism between absorption and effective hot electron collection.

Reference

- [1] M. W. Knight, H. Sobhani, P. Nordlander, N. J. Halas, “*Photodetection with Active Optical Antennas*,” *Science* 332, 702–704, (2011).
- [2] F. Wang, and N. A. Melosh, “*Plasmonic Energy Collection through Hot Carrier Extraction*,” *Nano Lett.* 11, 5426–5430, (2011).
- [3] Y. Nishijima, K. Ueno, Y. Yokota, K. Murakoshi, and H. Misawa, “*Plasmon-Assisted Photocurrent Generation from Visible to Near-Infrared Wavelength Using a Au-Nanorods/TiO₂ Electrode*,” *J. Phys. Chem. Lett.* 1, 2031–2036, (2010).
- [4] Y. K. Lee, et al. “*Surface Plasmon-Driven Hot Electron Flow Probed with MetalSemiconductor Nanodiodes*,” *Nano Lett.* 11, 4251–4255, (2011).
- [5] M. G. Walter, et al. “*Solar Water Splitting Cells*,” *Chem. Rev.* 110, 6446–6473, (2010).
- [6] J. B. Chou, Y. X. Yeng, Y. E. Lee, A. Lenert, V. Rinnerbauer, I. Celanovic, M. Soljačić, N. X. Fang, E. N. Wang, and Kim, S.-G, “*Enabling Ideal Selective Solar Absorption with 2D Metallic Dielectric Photonic Crystals*,” *Adv. Mater.*, 26: 8041–8045, (2014).
- [7] J. D. Joannopoulos, S. G. Johnson, J. N. Winn, R. D. Meade, *Photonic Crystals: Molding the Flow of Light*, Second edition, Princeton University Press, (2008).
- [8] A. D. Semenov, G. N. Gol’tsman, R. Sobolewski, “*Hot-electron effect in superconductors and its applications for radiation sensors*,” *Supercond. Sci. Technol.* 15, R1, (2002).
- [9] M. W. Knight, H. Sobhani, P. Nordlander, N. J. Halas, “*Photodetection with active optical antennas*,” *Science* 332, 702–704 (2011).

- [10] M. Moskovits, "Hot electrons cross boundaries," *Science* 332, 676–677 (2011).
- [11] C. Clavero, "Plasmon-induced hot-electron generation at nanoparticle/metal-oxide interfaces for photovoltaic and photocatalytic devices," *NATURE PHOTONICS*, 8, 98, (2014).
- [12] A. O. Govorov, H. Zhang, Y. K. Gun'ko, "Theory of Photoinjection of Hot Plasmonic Carriers from Metal Nanostructures into Semiconductors and Surface Molecules," *J. Phys. Chem. C*, 117 (32), 16616, (2013).
- [13] J.J. Quinn, "Range of Excited Electrons in Metals," *Phys. Rev.* 126, 1453 (1962).
- [14] R. N. Stuart, F. Wooten, W. E. Spicer, "Mean Free Path of Hot Electrons and Holes in Metals," *Phys. Rev. Lett.* 10, 119 (1963).
- [15] R. H. Fowler, "The analysis of photoelectric sensitivity curves for clean metals at various temperatures," *Phys. Rev.* 38, 45, (1931).
- [16] K. Yee, "Numerical solution of initial boundary value problems involving Maxwell's equations in isotropic media," *IEEE Trans. Antennas and Propagation* 14 (3): 302–307, (1966).
- [17] I. Valuev, A. Deinega, and S. Belousov, "Iterative technique for analysis of periodic structures at oblique incidence in the finite-difference time-domain method," *Opt. Lett.* 33: 1491, (2008).
- [18] A. Aminian and Y. Rahmat-Samii, "Spectral FDTD: a novel technique for the analysis of oblique incident plane wave on periodic structures," *IEEE Trans. Antennas and Propagation* 54: 1818, (2006).
- [19] A. Deinega, S. Belousov, and I. Valuev, "Hybrid transfer-matrix FDTD method for layered periodic structures," *Opt. Lett.* 34: 860, (2009).
- [20] Y. Hao and R. Mittra, *FDTD Modeling of Metamaterials: Theory and Applications*, Artech House Publishers, (2009).

- [21] J. D. Jackson, "*Classical Electrodynamics*," Third Edition, Wiley, 1999.
- [22] F. T. Ulaby, *Fundamentals of Applied Electromagnetics*, Fifth Edition, Pearson Prentice Hall, 304-308, (2006).
- [23] Hecht, E. *Optics*, 4 edn, Pearson, (2002),
- [24] J. Hao, L. Zhou, and M. Qiu, "*Nearly total absorption of light and heat generation by plasmonic metamaterials*," *Phys. Rev. B*, 83 (2011).
- [25] M. T. Hill, M. Marell, E. S. P. Leong, B. Smalbrugge, Y. Zhu, M. Sun, P. J. v. Veldhoven, E. J. Geluk, F. Karouta, Y.Oei, R. Nötzel, C. Ning, and M. K. Smit, "*Lasing in metal-insulator-metal sub-wavelength plasmonic waveguides*," *Opt. Express* 17, 11107-11112, (2009).
- [26] Z Han, E Forsberg, S He, "*Surface Plasmon Bragg Gratings Formed in Metal-Insulator-Metal Waveguides*," *Photonics Technology Letters, IEEE*, VOL. 19, NO. 2, 91, (2007).
- [27] T. J. Seok, A. Jamshidi, M. Eggleston, M. C. Wu, "*Mass-producible and efficient optical antennas with CMOS-fabricated nanometer-scale gap*," *Opt. Express*, 21, 16561, (2013).
- [28] X. Liu, X. Deng, P. Sciortino, M. Buonanno, F. Walters, R. Varghese, J. Bacon, L. Chen, N. O'Brien, J. J. Wang, "*Large Area, 38 nm Half-Pitch Grating Fabrication by Using Atomic Spacer Lithography from Aluminum Wire Grids*," *Nano Lett.*, 6, 2723, (2006).
- [29] D. S. Y. Hsu, N. H. Turner, K. W. Pierson, V. A. Shamamian, "*20 nm linewidth platinum pattern fabrication using conformal effusive-source molecular precursor deposition and sidewall lithography*," *J. Vac. Sci. Technol. B Microelectron. Nanometer Struct.*, 10, 2251, (1992).
- [30] B. Hoex, S. B. S. Heil, E. Langereis, M. C. M. van de Sanden, and W. M. M. Kessels,

“Ultralow surface recombination of c-Si substrates passivated by plasma-assisted atomic layer deposited Al₂O₃,” APPLIED PHYSICS LETTERS 89, 042112, (2006).

- [31] J. Schmidt, A. Merkle, R. Brendel, B. Hoex, M. C. M. van de Sanden, and W. M. M. Kessels, *“Surface passivation of high-efficiency silicon solar cells by atomic-layer-deposited Al₂O₃,” Prog. Photovolt: Res. Appl., 16: 461–466, (2008).*